



Numerical studies of metal particle behaviors inside the selective laser melting (SLM) chamber through computational fluid dynamics (CFD)

Sz-Jia Tzeng¹ · Xiang-Xin Chen¹ · Wei-Cheng Wang¹

Received: 17 December 2019 / Accepted: 22 April 2020 / Published online: 2 May 2020
© Springer-Verlag London Ltd., part of Springer Nature 2020

Abstract

The flow behavior of the shielding gas has been a key factor to improve the quality of products manufactured by the selective laser melting (SLM) technology as it is a major mechanism to remove the ejected metal particles away from the working plane. In this study, to obtain a proper flow field, computational fluid dynamics (CFD) with the application of the Taguchi method was employed to investigate the flow field across the working chamber, with the variations in the geometries of the blowing nozzle, the widths of the suction tunnel, the suction-to-plane distances, and the Reynolds numbers of the blowing flow. The simulation was first verified with experimental measurements. The ejecting motions of the metal powders were also taken into consideration to study the interactions between the shielding gas and the ejected particles. The results demonstrated that axis switching as well as the suction-to-plane distance are the important factors for improving the particle removal efficiency during the SLM operation.

Keywords Selective laser melting · 3-D printing · Computational fluid dynamics · Taguchi method · Particle removal efficiency · Axis switching

1 Introduction

Selective laser melting (SLM) is a turning process of additive manufacturing (AM) and has gradually taken over the traditional processes owing to its rapid prototyping, less material consumption, light material weight, and fine mechanical properties. The most dramatic industry in global AM development is aircraft manufacturing, rising by 10% in 17 years [1, 2]. The manufacturing process of SLM fuses the metallic powders by the high-energy laser beam layer by layer inside the working chamber with filling the well-controlled inert gas. However, the ejected powders from the melting mechanical part result in a significant instability of the process and this degrades the quality of the final SLM product [3].

Several parameters would increase the instability of the melting flow including the balling effect, melt splashing, etc. [4, 5]. Porosity and surface roughness are two primary targets determining the quality of the product produced by SLM

[4–7]. In order to obtain lower porosity and surface roughness for better product quality, one of the most crucial factors is the efficiency of the shielding gas [4, 7]. The functionalities of the shielding gas in SLM are not only for preventing the metal powder oxidation but also for providing the transportation to remove the ejected powders [8]. Ladewig et al. [3] conducted the experiments on an EOS Eosint M280 and indicated the detailed theoretical basics regarding the process by-products and their influences. They proposed that an undirected flow or a lower flow velocity caused beam attenuation and material re-deposition owing to the insufficient removal of the process by-product, resulting in the balling effect. Bidare et al. [9] also pointed out that an inward flow of the ambient gas with rapid momentum transfer was produced due to the intensive evaporation of the metal vapor in the plume region. The particles entrained by the flow are either removed or consolidated onto the track.

According to the authors' previous study [10], the design concepts for conducting the shielding gas were similar to the air curtain. The shielding gas was introduced into the working chamber through a vertical downward-blowing nozzle on the top of the working chamber and was drawn away downstream by two parallel suction tunnels. Parameters which affected the flow behaviors of the air curtain included geometries and

✉ Wei-Cheng Wang
wilsonwang@mail.ncku.edu.tw

¹ Department of Aeronautics and Astronautics, National Cheng Kung University, Tainan, Taiwan 70101

numbers of the blowing nozzle, pressure difference, temperature difference, Reynolds number, and so on [11–15]. Besides, the properties of the ejected particles should also be carefully taken into consideration in order to accurately discuss the interactions between fluids and particles.

Owing to the difficulties of experimentally observing the flow behaviors inside the SLM chamber, computational fluid dynamics (CFD) can be applied to deeply analyze the interactions between the shielding gas and the ejected particles. Masmoudi et al. [16] applied a CFD analysis to study the melt pool behaviors during the SLM operation and pointed out that the volume of the evaporated material can be controlled by adjusting the pressures of the shielding gas. Ferrar et al. [7] investigated the effects of the inert gas flow within the SLM process through CFD and found that the porosity can be improved by highly uniform flow. Aiming to systematically optimize the efficiency of the shielding gas among various parameters in the SLM chamber, the Taguchi method of the robust design, a well-known statistical method has been applied. For example, Calignano et al. [17] used the Taguchi method to investigate the degree of influence of each factor on surface roughness and obtained the optimal design of the direct metal laser sintering (DMLS). Kumar et al. [18] changed various control parameters including laser power, laser scan speed, and mass flow rate through the Taguchi method in order to predict the deposit depth in the direct metal deposition (DMD). According to the studies above, it was expected that a proper design of the SLM working chamber for obtaining appropriate flow behaviors can be achieved through the applications of CFD and the Taguchi method. However, a defined indication for determining the quality of the flow inside the SLM chamber and thus for judging the quality of the SLM process still remains the scientific gap. Therefore, in this study, a definition was added as a discriminative index, and the particle removal efficiency was used to determine the quality of the SLM process.

During SLM manufacturing, higher removal efficiency of ejected powders leads to better quality of the product. As a consequence, in order to establish the flow field with adequate momentum transfer to successfully remove the ejected powders, the numerical simulations through CFD accompanied with L9 orthogonal array of the Taguchi design were conducted. Multiple control factors such as the aspect ratios of the blowing nozzle, thicknesses of the suction tunnels, suction-to-plane distances, and Reynolds numbers of the blowing jet were considered.

2 Methodology

2.1 Numerical modeling

The commercial software CFD-ACE+ (version 2016.0.0.11820) was used to simulate the behaviors of the

flow and particles inside the SLM working chamber. The first-order upwind scheme and Semi-Implicit Method for Pressure-Linked Equations Consistent (SIMPLEC) algorithm were employed to solve the Navier-Stokes governing equations. The Energy Conservation Equation was mainly used to discretize and solve the heat transfer mechanism. The discrete particles were tracked through the computational domain through solving the Lagrangian equations.

The grids were generated in CFD-GEOM (version 2016.0.0.17). The geometry of the physical domain, as shown in Fig. 1, was sized at 700 mm (length) \times 1495 mm (width) \times 500 mm (height), including one blowing nozzle on the top and two suction tunnels at both sides of the working chamber. As shown in Fig. 2, structured grids were generated for the entire model apart from the irregular area such as the blowing nozzle and the corners in the suction devices, for the purpose of obtaining better convergence. The meshes along the Z-direction away from the working plane ($Z \geq 300$ mm and $Z \leq -300$ mm) were gradually dispersed and reduced under the power law to avoid computational expanses. Based on the grid independence study carried out in our previous study [10], the numbers of grids of 1,710,000 have been proved to obtain the best match to the experimental results, which can be employed in this simulation. Additionally, based on the cross-validation results obtained from our previous studies [10, 19], Menter's Shear Stress Transport (SST) K Omega was chosen to be the most suitable turbulence model to simulate the flow phenomena.

2.2 Modules and boundary conditions

This study not only investigated the flow field but also took the heat transfer and the motions of ejected powder into consideration. The flow was assumed to be three

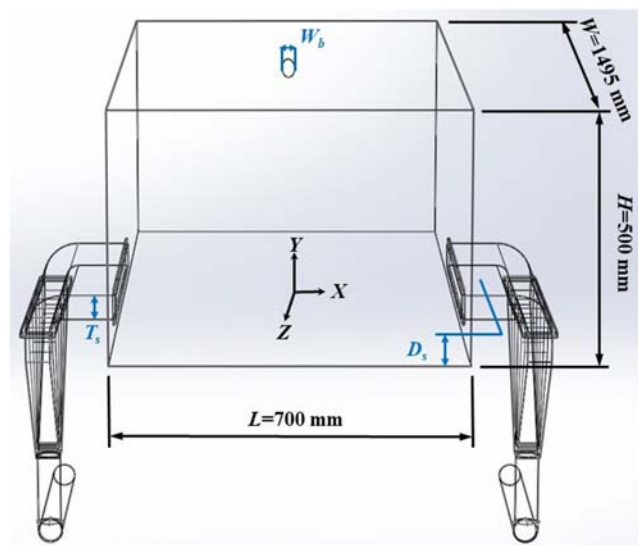


Fig. 1 Definitions of geometric parameters

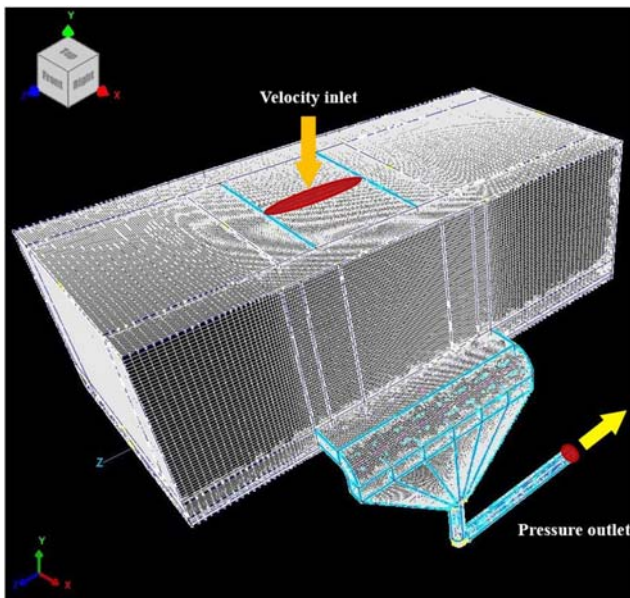


Fig. 2 Meshes and boundary conditions

dimensional, steady, turbulent, incompressible, and ideal gas. The computational settings conducted for the simulation are summarized in Table 1. Nitrogen was designated as the working fluid, and the density was assumed to follow the incompressible ideal gas law. The specified default reference pressure was set as $100,000 \text{ N/m}^2$ ($\sim 1 \text{ bar}$) which corresponded to the one reported by Masmoudi et al. [16], proposing that higher ambient pressure squeezed the volume and the velocity of the evaporated material. Steady-state condition was used to analyze the initial flow field, and the flow rates of the inflow and outflow were fixed because the SLM chamber was designed to be the circulatory system. Therefore, the velocities of the two outlets varied with the inlet velocities, which depended on the various combinations of the Reynolds numbers and the areas of the blowing nozzle.

The velocity inlet and pressure outlet calculated through the Bernoulli equation were used for better convergence. The obtained steady results of the flow behaviors were imported into the transient state under 0.0001 s time step as the initial condition to observe the gas-powder interactions. The SUS-304 material was selected as the wall material of the working chamber and was considered to be adiabatic. The working plane was heated at a constant heat source of $10,000 \text{ W/m}^2$ before starting the manufacturing in order to achieve the temperature of the actual SLM process and eliminate the thermal stress. The spray module was used to analyze the interactions between the shielding gas and the ejected particles, using one-way (continuous phase to discrete phase) to exchange the momentum, energy and mass. The equations between the flow and the ejected particles are shown as follows:

$$m_p \frac{d\vec{V}}{dt} = C_D \rho \left(\vec{U} - \vec{V} \right) \left| \vec{U} - \vec{V} \right| \frac{A_d}{2} + m_p g + S_m \quad (1)$$

where m_p and \vec{V} are the mass and velocity vectors of the particles, C_D is the drag coefficient, ρ is the density of the surrounding gas, \vec{U} is the velocity of the surrounding gas, A_d is the particle frontal area, and S_m is the additional mass source. The material of the powders was chosen as titanium alloy, and the diameters of those before the process were $\leq 35 \mu\text{m}$. Previous literatures were referenced for simulating the interactions between gas fluid and powders. Romano et al. [20] predicted the temperature distributions of different material powders in the SLM process and exhibited that the titanium had the highest local temperatures approximately from 2660 to 3382 K. Ly et al. [8] presented the ejecting velocities experimentally and numerically and classified the ejected particles into three types: 60% hot entrainment ejections with velocities of 6–20 m/s, 25% cold entrainment ejections with velocities of 2–4 m/s, and 15% recoil pressure-induced droplet-breakup ejections with velocities of 3–8 m/s. The ejection angles depending on the scan speed of the laser beam changed from nearly vertical to approximately 47° from the vertical while increasing the scan speeds from 0.5 to 1.5 m/s. Furthermore, the diameters of entrained particles were larger than the original size distributions due to the recoil pressure. Qiu et al. [5] also proposed that the scattering velocity rose from 2.2 to 15 m/s while the laser scan speed was increased from 2.3 to 3.5 m/s. Table 2 summarizes the previous literatures on the powder properties used for simulating the ejected powders fused by the high-energy laser beam in the SLM chamber [5, 8, 9, 20, 21].

2.3 Taguchi method

The Taguchi method was used to determine an optimal design concept among all the design parameters for the SLM working chamber. The L9 orthogonal array of the Taguchi design has been applied in order to efficiently explore a large number of parameter changes and establish the optimal design parameters. According to our previous results [10], the elliptical shape for the blowing nozzle was selected owing to its better flow uniformity and higher momentum exchange compared to other blowing nozzle geometries. It was employed in this simulation with different aspect ratios (ARs) as the major axis was fixed to 300 mm, half of the length of the suction tunnel. Figure 3 and Table 3 show the geometries of the elliptical nozzle for three levels as well as four control factors

Table 1 Computational parameters for simulating the working chamber

Modules	Option settings	
Flow turbulence	Turbulence model	SST K Omega
	Wall function	Standard wall
	Time dependence	Transient
	Time step (s)	0.0001
	Gravity in Y-direction (m/s ²)	− 9.81
	Pressure (N/m ²)	100,000
	Fluid	N ₂
	Inlet boundary type	Velocity inlet
	Outlet boundary type	Pressure outlet
	Spatial differencing method—velocity	1st order
	Spatial differencing method—turbulence	1st order
	Linear solver	AMG
	Residual error	1 × 10 ^{−4}
	Min. residual	1E−018
	Inertial relaxation	0.2
	Linear relaxation	0.6
Heat transfer	Fluid	
	Specific heat (J/kg-K)	1007
	Thermal conductivity (W/m-K)	0.0263
	Wall	
	Subtype	Adiabatic
	Thermal conductivity (W/m-K)	16.3
	Thickness (m)	0.003
	Roughness height (m)	1.5E−005
Spray	Heat source (W/m ²)	10,000
	Drag between particle and fluid	
	Exchange heat with the surrounding fluid	
	Boundary treatment	Stick
	Injection frequency	5000

including the widths of the blowing nozzle (W_b), the thicknesses of the suction tunnel (T_s), the suction-to-plane distances (D_s), and the Reynolds numbers (Re). The simulation layout for L9 is shown in Table 4.

The signal-to-noise (S/N) ratios are the log functions regarded as the prominent targets to analyze the results. The S/N ratio can be divided into three categories: the smaller the better, the larger the better, and on target (minimum variation). Since the goal of this study was to remove most of the ejected particles, the larger the better was used and S/N ratios can be calculated by

$$\eta_L = -10 \log \left[\frac{1}{n} \sum \left(\frac{1}{y_i^2} \right) \right] \quad (2)$$

where η_L denotes the S/N ratios, n is the number of tests, and y_i represents the observed values of the i th sample.

2.4 Particle removal efficiency

The particle removal efficiency is the primary indicator in this study to explore the interactions between the ejected particles and the flow field of the shielding gas. In the real SLM working chamber, the number of lasers is increased from one to four since the working chamber was scale-up. Hence, the working plane explored was divided into four regions with an area of 250 mm × 250 mm each. As Fig. 4 shows, the titanium alloy powders assumed to be fused by the laser beam were about to eject with the physical property arrangements presented in

Table 2 Hypothetical properties of the ejected powders

Species	Temperature	Diameters	Ejection velocities
Titanium alloy	3000 K	20~80 μm	2~15 m/s

Fig. 3 Geometries of the elliptic nozzle with three different minor axis lengths. **a** Level 1, **b** level 2, **c** level 3

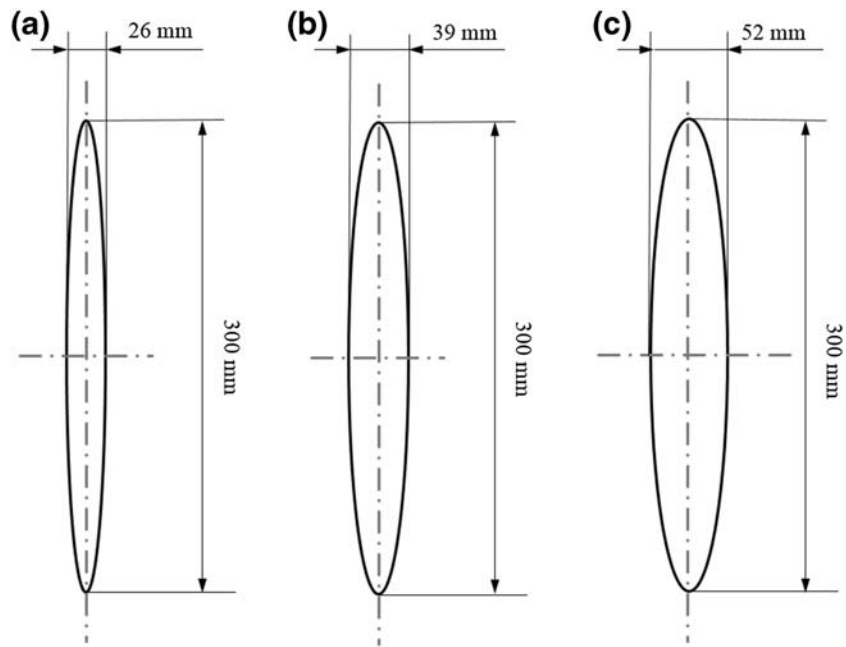


Table 2. The powders were initially spread all over the working plane and were presented in four different colors which represent four regions. A simplified number of particles was used to match the simulation time and the computational specifications. Although it cannot be exactly the same as the actual SLM process, it was sufficient to exhibit the capability of particle removal through the flow field at various regions. The removed particles were characterized as those particles were carried away from the working plane by the carrier flow. The removal efficiency (R_p) of the ejected particles was defined as

$$R_p = \frac{\text{numbers of the removed particles}}{\text{numbers of the initial spread particles}} \times 100\% \quad (3)$$

3 Results and discussion

3.1 Cross-validation with experiment

The simulation carried out in this study was first validated with the experiment conducted through particle image velocimetry (PIV) measurement, the details of which can be

Table 3 Control factors and levels

Parameters	Level 1	Level 2	Level 3
Width of the blowing nozzle (W_b) (mm)	26	39	52
Thickness of the suction tunnels (T_s) (mm)	47	44	50
Suction-to-plane distance (D_s) (mm)	26.5	30	23
Reynolds number (Re)	27,000	40,000	54,000

found in the authors’ previous study [10]. The simulated parameters were set as $W_b = 26$ mm, $T_s = 47$ mm, $D_s = 26.5$ mm, $Re = 3600$, and $Re_{out} = 6000$ to verify with the experiment. In this case, the flow rate at the outlet was greater than the flow at the inlet. The Reynolds numbers at the outlet were defined as

$$Re_{out} = V_p d / \nu \quad (4)$$

where V_p is the velocities measured in the pipes at both sides, d is the diameter of the pipe, and ν is the air kinematic viscosity. Three regions from the blowing nozzle to the working plane were selected according to the previous study [22]: the region of flow establishment, the established region, and the impingement region, as shown in Fig. 5. The impingement region was chosen for this cross-validation to investigate the particle removal efficiency above the working plane. Figure 6 shows the centerline velocity (V) distribution across the impingement

Table 4 Full factorial designs with L9 orthogonal array

Number of samples	W_b	T_s	D_s	Re
1	1	1	1	1
2	1	2	2	2
3	1	3	3	3
4	2	1	2	3
5	2	2	3	1
6	2	3	1	2
7	3	1	3	2
8	3	2	1	3
9	3	3	2	1

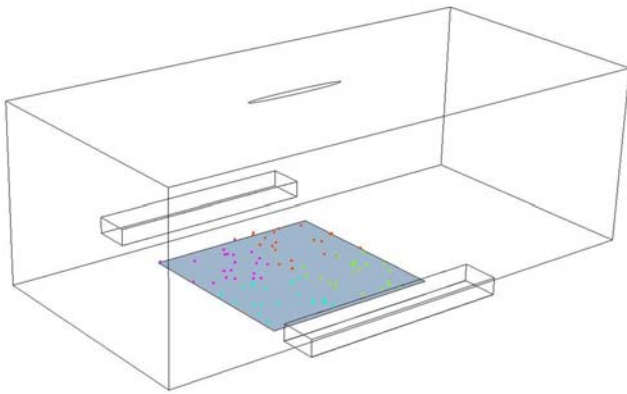


Fig. 4 Initial particle distributions over the SLM working plane

region, which was gradually decreased along the negative y -direction and then the stagnation point was formed. Part of the momentum was lost while most of the axial momentum was transferred to the radial momentum. The comparisons of simulated and experimental velocity distributions in the x -direction for the cases of $x = 0.15$ m, 0.20 m, and 0.25 m are shown in Fig. 7. The boundary layer grows as the jet impinges onto the working plane. Meanwhile, the flow was affected by the strength of the suction tunnel, leading to the flow separation and movement along the x -direction. It was found that the velocity (U) obtained the maximum value at the impingement region further downstream where H was around 0.005 m. After that, the velocity started decreasing and slightly rolled up as it was close to the suction tunnel. As shown in Figs. 6 and 7, the velocity profiles at both x -dir and y -dir obtained through the simulations agreed well with the experimental results.

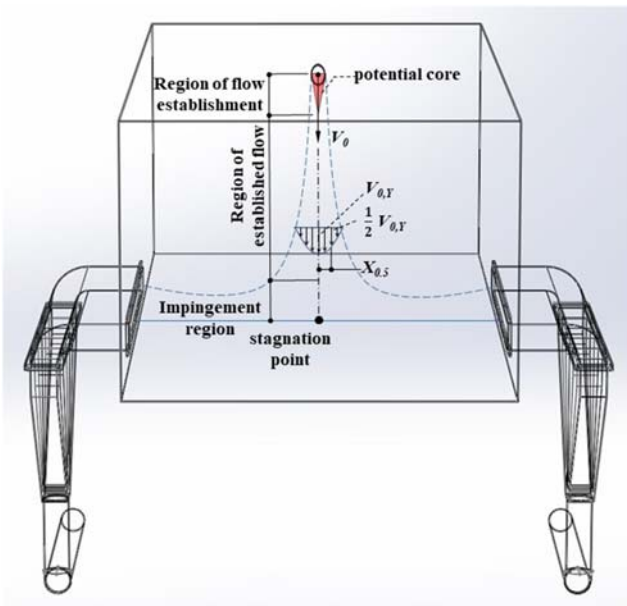


Fig. 5 Schematic representation of the impinging jet

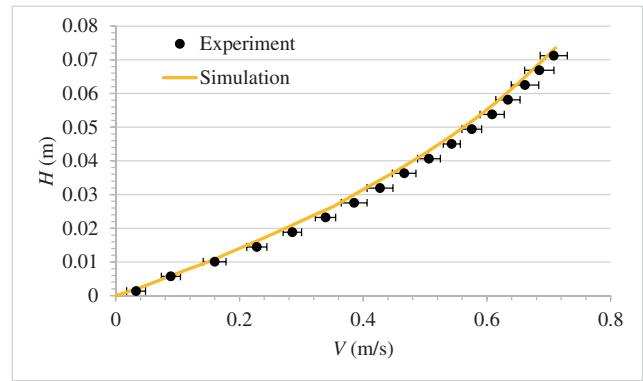
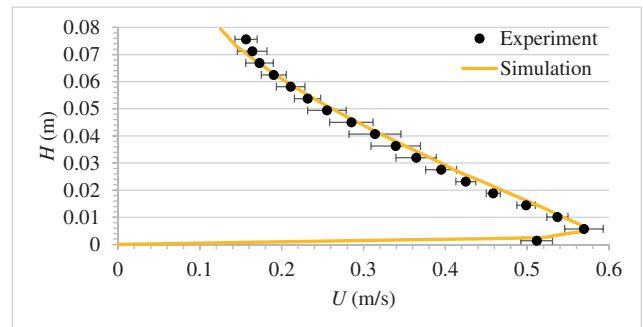


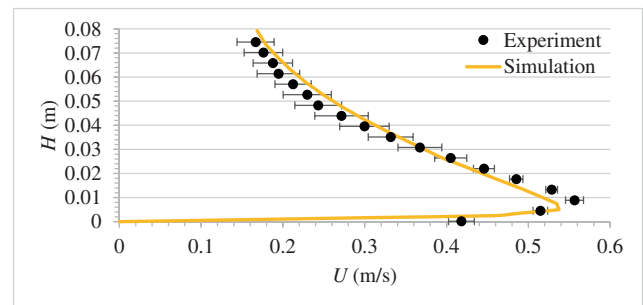
Fig. 6 Centerline velocity distribution across the impingement region

3.2 Decay and spread of the main jet flow

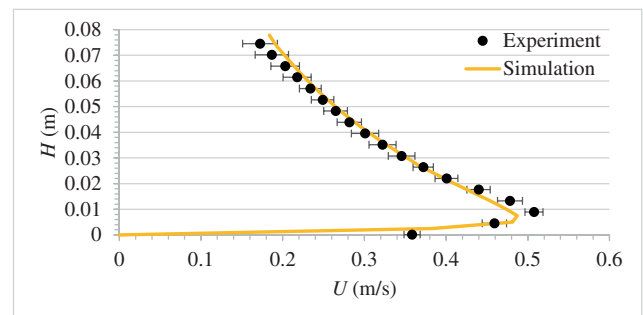
The velocity decay and spread rate, which strongly depend on the entrainment effect, are the primary characteristics for



(a)



(b)



(c)

Fig. 7 Comparisons of the velocity profiles obtained through simulation and experiment. a $X = 0.15$ m; b $X = 0.20$ m; c $X = 0.25$ m

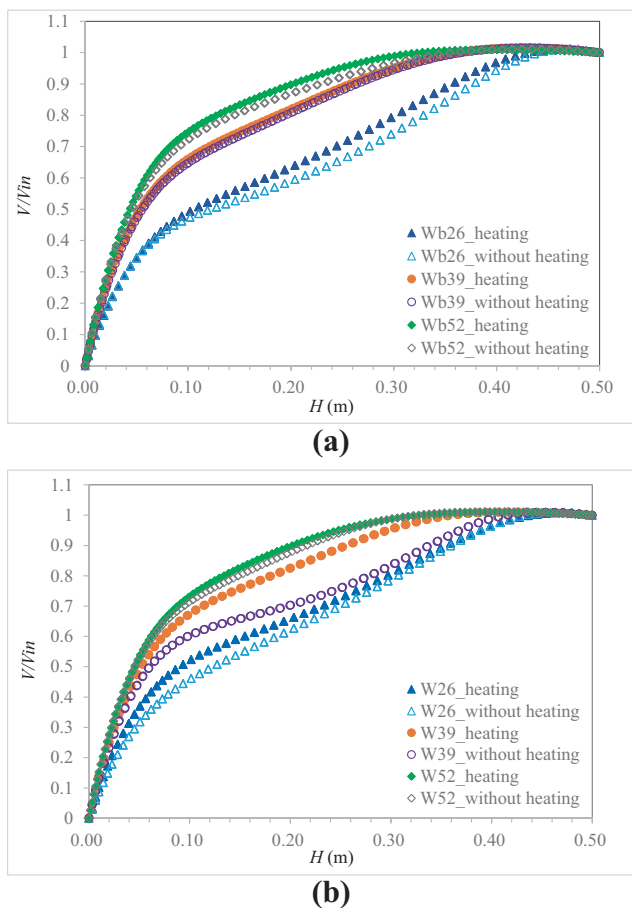


Fig. 8 Mean streamwise velocity decay along the jet centerline at **a** $Re = 27,000$ and **b** $Re = 54,000$

investigating the jet flow. The velocity decay is a phenomenon in which the velocity decreases from the nozzle outlet to the downstream. The spread rate (K_y) of the jet was defined as follows:

$$K_y = \frac{\partial X_{0.5}}{\partial Y} \tag{5}$$

Table 5 The results for removal efficiencies and S/N ratio values

Number of samples	Control factors				R_p S/N ratios (%) (dB)	
	W_b (mm)	T_s (mm)	D_s (mm)	Re		
1	26	47	26.5	27,000	75.00	37.40
2	26	44	30.0	40,000	81.55	38.05
3	26	50	23.0	54,000	77.98	37.52
4	39	47	30.0	54,000	82.14	38.19
5	39	44	23.0	27,000	70.24	36.61
6	39	50	26.5	40,000	76.19	37.55
7	52	47	23.0	40,000	75.00	37.05
8	52	44	26.5	54,000	75.00	37.35
9	52	50	30.0	27,000	73.81	37.27

These are the main concerns for understanding the flow structure inside the SLM chamber. As shown in Fig. 8, it can be seen that the centerline velocity slightly accelerated after leaving the blowing nozzle, due to the vena contracta effect. The velocity decays and spread rates were relatively lower than the ones in the impingement region. The jet flow started mixing with the ambient fluid and spread over intensively. The vortices emerged thereafter. Hence, the velocity decayed along the jet centerline and the radial momentum increased while it developed further downstream. Moreover, vortex rollups were delayed and energy dissipations reduced owing to the high suction velocity [19]. Figure 8 presents the velocity decay along the jet centerline with various minor axis lengths of the blowing nozzle. The W_b were 26, 39, and 52 mm, corresponding to the ARs of 11.54, 7.69, and 5.77 respectively. Heating the working plane was also taken into consideration.

It can be observed that the elliptic jet with a larger aspect ratio has faster velocity decay and higher spread rates, which were consistent with the previous studies [12, 22]. In addition, the centerline velocity was slightly increased toward the working plane when the heating was applied to the plane due to the heat convection. This resulted in relatively slower velocity decay for the jet flow with heating compared to the one without heating. Moreover, Reynolds numbers have little influence on the velocity decay and the velocity profiles with the Reynolds numbers of 27,000 and 54,000 behaved similarly.

3.3 Optimization of the working chamber through Taguchi analysis

3.3.1 Analysis of variance

Table 5 shows the simulation results of the removal efficiencies calculated through Eq. (3) as well as the corresponding S/N ratios obtained using Eq. (2). Among the 9 cases designed by the L9 orthogonal array, case 4 with $W_b = 39$ mm, $T_s =$

Table 6 Mean S/N response table for R_p

Level	The-larger-the-better S/N (dB)			
	W_b	T_s	D_s	Re
Level 1	37.66	37.55	37.43	37.09
Level 2	37.45	37.34	37.84	37.55
Level 3	37.22	37.45	37.06	37.69
Delta	0.44	0.21	0.78	0.60
Rank	3	4	1	2

47 mm, $D_s = 30$ mm, and $Re = 54,000$, which has the largest S/N ratio of 38.19 dB, obtained the best particle removal efficiency of 82.14%. The average S/N response value for each factor is presented in Table 6. To inquire the degree of influence for each factor, delta statistics (to indicate the relative effect of each factor on the response) have been applied to compute the rank, which is the maximum average S/N value minus the minimum one. A larger delta value represented the higher influence of the factor. Hence, rank 1 with the highest delta value has the most significant influence. As shown in Table 6, suction-to-plane distance (D_s) has the highest impact on the particle removal efficiency, followed by the Reynolds

number and the width of the blowing nozzle. The thickness of the suction tunnel, in this case, has the lowest impact on the particle removal efficiency. Figure 9 shows the overall S/N response graph, which was used to determine better control factors for improving the removal efficiency. A larger S/N ratio represented higher particle removal efficiency; therefore, within the selected control factors, the predicted optimal parameters for the SLM chamber were determined as the width of the blowing nozzle at level 1 (26 mm), the thickness of the suction tunnels at level 1 (47 mm), the suction-to-plane distance at level 2 (30 mm), and the Reynolds number at level 3 (54,000).

3.3.2 Confirmation test

The improvements of particle removal efficiency with application of the optimal factors obtained in the last section were verified in this section. Table 7 shows the comparisons of the results between the simulated and experimental values. The estimated S/N value $\hat{\eta}$ using the optimal control factors was calculated as

$$\hat{\eta} = \bar{\eta} + \sum_{i=1}^q (\bar{\eta}_i - \bar{\eta}) \quad (6)$$

Fig. 9 The effects of design parameters on the average S/N ratio for R_p

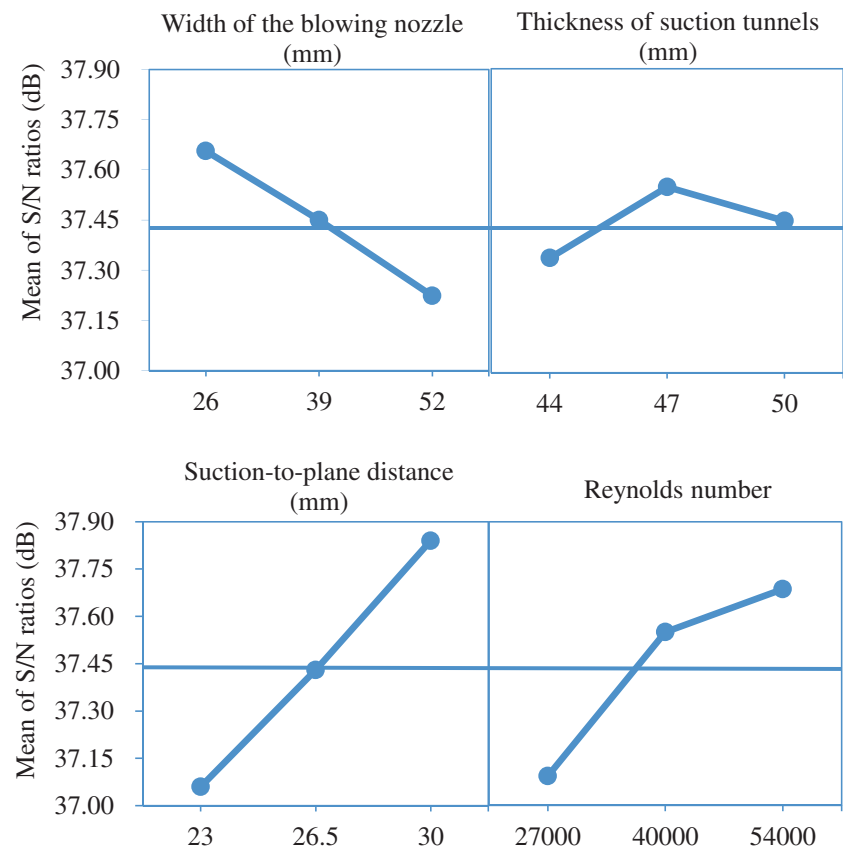


Table 7 Optimizing responses (max R_p), predicted and experimental values

Optimal factors				Predicted		Experiment [23]	
W_b (mm)	T_s (mm)	D_s (mm)	Re	R_p (%)	S/N (dB)	R_p (%)	S/N (dB)
26	47	30	54,000	83.14	38.40	82.73	38.35

where $\bar{\eta}$ is the total mean S/N ratios, $\bar{\eta}_i$ is the mean S/N ratio at the optimal level, and q is the number of the design control factor that affected the quality characteristics significantly. It can be seen from Table 7 that the simulation results agreed well with the experimental ones, confirming the optimal design through the Taguchi analysis. As a consequence, the increment of the S/N ratio from the initial parameters ($W_b = 26$ mm, $T_s = 47$ mm, $D_s = 26.5$ mm, and $Re = 27,000$) was 0.95 dB, which improved the particle removal efficiency from 75 to 82.73%.

3.4 Axis switching

Axis switching is a universal phenomenon which can be found in the slender geometry of the nozzle because the jet expanding in the minor plane is higher than the one in the major plane [11–13, 24]. To investigate the influences of the axis switching on the flow behaviors inside the SLM working chamber, the working plane was divided into four quadrants, Q1, Q2, Q3, and Q4, each with a size of 250 mm \times 250 mm at $H = 0.04$ m as shown in Fig. 10. Because of the axis-switching phenomenon, the velocity distributions in Q2 and Q4 were faster than those in Q1 and Q3, attributed to the stronger momentum strength. The dominant quadrants in Q2 and Q4 of the elliptical jet spreading have also been observed by Aleyasin et al. [12]. On the other hand, the weaker momentum strength in Q1 and Q3 lowered the particle removal efficiency.

To improve the velocity gaps between Q1 and Q4 as well as Q2 and Q3, the velocity settings of both suction tunnels were suggested to be divided into two sections with two different outlet velocities by increasing the outlet velocities at Q1 and Q3 as well as reducing the outlet velocities at Q2 and Q4 meanwhile. Through the modifications of the outlet velocities, the axis switching can be resolved and the particle removal efficiency was increased by 1.2% (to 83.93%).

4 Conclusion

Continuing from the authors' previous study, more influencing factors were taken into consideration for improving the flow behaviors inside the SLM working chamber and this improves the quality of the SLM manufacturing, including the heating module, particle ejections, aspect ratios, and Reynolds numbers. Through the CFD analysis accompanied

with the Taguchi method, optimal parameters (within the selected control factors) for designing the SLM working chamber were determined. The simulated velocity profiles with SST K Omega turbulence model were first successfully validated with the experiment results. The aspect ratio of the blowing nozzle was found to be significant to the flow development. The elliptic jet with a shorter minor axis was observed to have a faster velocity decay and spreading rate. Through the optimizing analysis, the S/N ratio indicated that the suction-to-plane distance has the greatest impact on the particle removal efficiency.

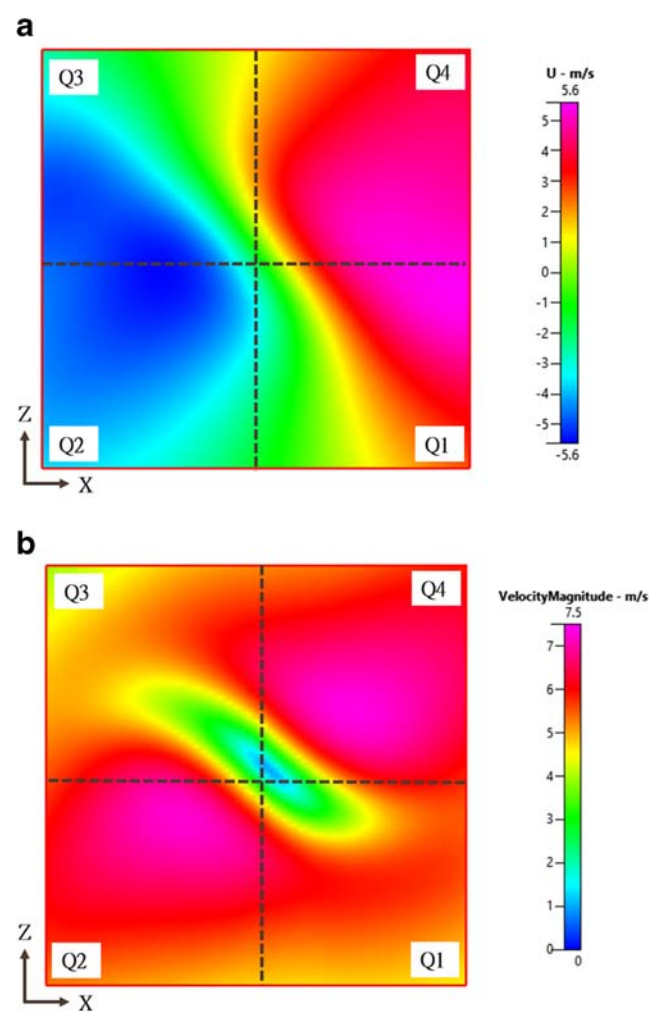


Fig. 10 Velocity distributions within the impingement region above the working plane. **a** U , **b** velocity magnitudes of U , V , and W

The proper conditions for enhancing the particle removal efficiency were found to be 26 mm for the width of the elliptic nozzle, 47 mm for the thickness of suction tunnels, 30 mm for the suction-to-plane distance, and 54,000 for the Reynolds number. As a primary characteristic, axis switching enhances the jet mixing which appropriately benefits the flow field inside the SLM working chamber. However, this leads to a non-uniform momentum distribution across the working plane. This defect can be improved by decreasing the suction strength between the two dominant quadrants Q2 and Q4 as well as increasing the suction strength between the other two quadrants Q1 and Q3.

Acknowledgments This project was supported by the Ministry of Science and Technology, Taiwan, through grant 107-2622-E-006-012-CC3.

References

1. WOHLERS, Wohlers associates, 2017
2. Borbás L (2013) Economical investigation of rapid prototyping, vol 3
3. Ladewig A, Schlick G, Fisser M, Schulze V, Glatzel U (2016) Influence of the shielding gas flow on the removal of process by-products in the selective laser melting process. *Addit Manuf* 10:1–9
4. Kuo T-Y, Lin Y-D (2007) Effects of different shielding gases and power waveforms on penetration characteristics and porosity formation in laser welding of Inconel 690 alloy. *Mater Trans* 48:219–226
5. Qiu C, Panwisawas C, Ward M, Basoalto HC, Brooks JW, Attallah MM (2015) On the role of melt flow into the surface structure and porosity development during selective laser melting. *Acta Mater* 96:72–79
6. Dai D, Gu D (2014) Thermal behavior and densification mechanism during selective laser melting of copper matrix composites: simulation and experiments. *Mater Des* 55:482–491
7. Ferrar B, Mullen L, Jones E, Stamp R, Sutcliffe C (2012) Gas flow effects on selective laser melting (SLM) manufacturing performance. *J Mater Process Technol* 212:355–364
8. Ly S, Rubenchik AM, Khairallah SA, Guss G, Matthews MJ (2017) Metal vapor micro-jet controls material redistribution in laser powder bed fusion additive manufacturing. *Sci Rep* 7:4085
9. Bidare P, Bitharas I, Ward R, Attallah M, Moore A (2018) Fluid and particle dynamics in laser powder bed fusion. *Acta Mater* 142:107–120
10. Chen X-X, Tzeng S-J, Wang W-C (2019) Numerical and experimental observations of the flow field inside a selective laser melting (SLM) chamber through computational fluid dynamics (CFD) and particle image velocimetry (PIV). *Powder Technol*
11. Zhao W, Kumar K, Mujumdar AS (2004) Flow and heat transfer characteristics of confined noncircular turbulent impinging jets. *Dry Technol* 22:2027–2049
12. Aleyasin SS, Tachie MF, Koupriyanov M (2017) Statistical properties of round, square, and elliptic jets at low and moderate Reynolds numbers. *J Fluids Eng* 139:101206
13. Reodikar SA, Meena HC, Vinze R, Prabhu SV (2016) Influence of the orifice shape on the local heat transfer distribution and axis switching by compressible jets impinging on flat surface. *Int J Therm Sci* 104:208–224
14. Elicer-Cortés J, Demarco R, Valencia A, Pavageau M (2009) Heat confinement in tunnels between two double-stream twin-jet air curtains. *Int Commun Heat Mass Transfer* 36:438–444
15. Wang LL, Zhong Z (2014) An approach to determine infiltration characteristics of building entrance equipped with air curtains. *Energy Build* 75:312–320
16. Masmoudi A, Bolot R, Coddet C (2015) Investigation of the laser–powder–atmosphere interaction zone during the selective laser melting process. *J Mater Process Technol* 225:122–132
17. Calignano F, Manfredi D, Ambrosio EP, Iuliano L, Fino P (August 01 2013) Influence of process parameters on surface roughness of aluminum parts produced by DMLS. *Int J Adv Manuf Technol* 67: 2743–2751
18. S. Kumar, A. K. S. Choudhary, J. Anwar, and V. Sharma, Optimization of process parameters in direct metal deposition technique using Taguchi method, 2016
19. Wang W-C, Chang C-Y (2017) Flow analysis of the laminated manufacturing system with laser sintering of metal powder. Part I: flow uniformity inside the working chamber. *Int J Adv Manuf Technol* 92:1299–1314
20. Romano J, Ladani L, Razmi J, Sadowski M (2015) Temperature distribution and melt geometry in laser and electron-beam melting processes – a comparison among common materials. *Addit Manuf* 8:1–11
21. Khairallah SA, Anderson AT, Rubenchik A, King WE (2016) Laser powder-bed fusion additive manufacturing: physics of complex melt flow and formation mechanisms of pores, spatter, and denudation zones. *Acta Mater* 108:36–45
22. Khayrullina A, van Hooff T, Blocken B, van Heijst G (2017) PIV measurements of isothermal plane turbulent impinging jets at moderate Reynolds numbers. *Exp Fluids* 58:31
23. Chen X-X (2018) Flow field analysis with the application of particle image velocimetry (PIV) system inside the selective laser melting (SLM) chamber, MS Thesis, Department of Aeronautics and Astronautics, National Cheng Kung University
24. Sforza PM, Steiger MH, Trentacoste N (1966) Studies on three-dimensional viscous jets. *AIAA J* 4:800–806

Publisher's note Springer Nature remains neutral with regard to jurisdictional claims in published maps and institutional affiliations.